

¹Hawai‘i Institute of Geophysics and Planetology, School of Ocean and Earth Science and Technology, University of Hawai‘i at Mānoa, HI, USA. E-mail: attias@hawaii.edu; cshuler@hawaii.edu; hdulaiov@hawaii.edu

²Scripps Institution of Oceanography, University of California San Diego, CA, USA. E-mail: sconstable@ucsd.edu

³Frontier Geosciences, BC, Canada. E-mail: dallas_sherman@frontiergeo.com

⁴University Malaysia Terengganu, Malaysia. E-mail: k.ismail@umt.edu.my

⁸ Freshwater plume imaging by CSEM data inversion

⁹ *Eric Attias¹, Steven Constable², Dallas Sherman³, Khaira Ismail⁴, Christopher Shuler¹,*
¹⁰ *and Henrietta Dulai¹*

¹¹

ABSTRACT

Submarine groundwater discharge (SGD) is an important mechanism that governs the hydrological cycle at the land-to-ocean transition zone. SGD is often manifested as cold surface water containing a substantial influx of nutrients, carbon, and solutes, thus altering the coastal areas’ oceanographical and biochemical properties. Due to the high spatial distribution and variability of SGD at the sea surface, it is nontrivial to map SGD seep location and fluxes using traditional oceanographic methods. This study presents regional-scale controlled-source electromagnetic (CSEM) high-resolution imagining of water-column freshwater plumes, offshore west of Hawai‘i Island. Our 2-D CSEM inversion models detect multiple vertical freshwater plumes (SGD point-sources) extending from the seafloor to the sea surface and imaged spatially distributed surface SGD. The resistivity of these freshwater plumes and surface SGD ranges from ~1.5 to 30 Ω m, extending to a distance of ~3 km offshore the Kailua-Kona coastline, Hawai‘i. Our plume-scale resistivity to salinity calculation indicates a substantial volume of freshwater occupies these plumes. This study demonstrates the CSEM techniques’ capability to detect and delineate freshwater plumes on a local scale and surface freshwater on a regional scale. Our findings provide valuable information to elucidate hydrogeological and oceanographic processes affecting west of Hawai‘i coastal waters biogeochemical cycle.

INTRODUCTION

¹³ Freshwater resources are essential for preserving public health, agricultural yields, economic
¹⁴ and ecosystem functions (e.g., [Gleick and Palaniappan, 2010](#); [Moosdorf and Oehler, 2017](#)).
¹⁵ As populations and economies grow, new constraints on water resources emerge that might
¹⁶ limit global water availability. Seeking alternative freshwater resources is vital to comply
¹⁷ with the global demand increase and, therefore, position groundwater research at the center
¹⁸ of broad interdisciplinary interest from industry, government, and academic organizations.

For the past decade, substantial evidence suggests that vast offshore groundwater reserves exist globally in submarine provinces that extend far beyond their associated coastline aquifers (e.g., Post et al., 2013; Knight et al., 2018; Gustafson et al., 2019; Micallef et al., 2020). The global occurrence of submarine groundwater can be found at an offshore distance that ranges from few hundred meters up to few hundred kilometers (e.g., Hathaway et al., 1979; Johnston, 1983; De Carlo, 1992; Mora, 2005), accumulating mostly at water depths of <100 m (e.g., Person et al., 2003; Grasby et al., 2009; Varma and Michael, 2012), extending from several meters below the seafloor (mbsf) up to a depth of ~4 km (e.g., Varma and Michael, 2012; van Geldern et al., 2013). These Offshore groundwaters are increasingly being recognized as a potential water resource for coastal communities (e.g., Cohen et al., 2010; Bakken et al., 2012; Jiao et al., 2015). Offshore submarine groundwater domains are frequently detected by a process known as submarine groundwater discharge (SGD), where fresh groundwater percolate upward from the sub-seafloor towards the water-column, and thus, alter the water-column salinity and temperature patterns (e.g., Church, 1996; Moore, 2010). Coastal SGD occur globally at various geological settings (e.g., Stieglitz, 2005; Kim and Kim, 2011; Knee et al., 2016; Prakash et al., 2018; Paldor et al., 2019).

Fresh SGD is commonly associated with oceanographic, hydrogeological, and environmental processes such as chemical weathering, ocean eutrophication, and climate change. SGD transports freshwater, carbon, nutrients, pollutants, metals, dissolved chemicals, and rare elements from continents to oceans on a broad spatial distribution as it is heterogeneous and diffusive (e.g., Moore, 2010; Kim and Kim, 2011; Taniguchi et al., 2019; Luijendijk et al., 2020). Fresh SGD affects coastal waters biogeochemical cycles, productivity, biomass, species composition, and zonation (e.g., Johannes, 1980; Moore, 2010; Sawyer et al., 2016), posing a risk for coastal water quality and ecosystems (Luijendijk et al., 2020), thus, has societal importance for coastal communities (Moosdorf and Oehler, 2017). The locations and rates of coastal SGD are essential to define boundary conditions and mixing dynamics in coastal aquifer models and characterize nutrients/contaminants transport to the marine environment (Duarte et al., 2006). Additionally, the fresh portion of SGD is critical, as it potentially buffers ocean acidification with groundwater alkalinity (e.g., Slomp and Van Cappellen, 2004; Cyronak et al., 2013). Fresh SGD is commonly studied using various geophysical, geochemical, bio-ecological, and numerical simulations methods, which utilize seepage meters, piezometers, natural tracers, water balance approach, and hydrograph separation techniques (e.g., Burnett et al., 2006; Moore, 2010; Taniguchi et al., 2019; Rosenberry et al., 2020). Nevertheless, it is not trivial to continuously map coastal SGD plumes in high-resolution due to the broad spatiotemporal variability of flow; therefore, direct measurements are scarce (e.g., Duarte et al., 2006; Burnett et al., 2006; Luijendijk et al., 2020).

surface SGD calculation derived from radon measurements collected in Kiholo Bay (west of Hawai'i, Figure A-1) infer a daily SGD discharge that varies between 1600–13,700 m³/d (Dulai et al., 2016). These SGD fluxes are comparable with an SGD study (using natural geochemical tracers), which suggests an average SGD fluxes range of 1,100 m³/d–12,000 m³/d (Peterson et al., 2009). Both of these studies offer estimations of SGD fluxes calculated from surface measurements conducted along the Kailua-Kona coastline; however, they do not provide information about the exact seafloor position of freshwater seepage. Therefore, SGD plume locations, as well as plume-specific spatial distribution and volumetric inventory (seafloor to sea-surface), are poorly constrained offshore west of Hawai'i.

Marine controlled-source electromagnetic (CSEM) methods have proven useful in imaging fresh to brackish groundwater subsurface accumulations at sedimentary regions (Müller

et al., 2011; Evans and Key, 2016; Haroon et al., 2018; Gustafson et al., 2019; Micallef et al., 2020; Lippert and Tezkan, 2020), as they are sensitive to contrasts in bulk electrical resistivity resulting from pore water salinity (e.g., Edwards, 2005; Constable, 2010). However, CSEM data inversion has never been used to image freshwater plumes within the water column. This study demonstrates, for the first time, the CSEM techniques' capability to image and delineate freshwater plumes from the seafloor to surface in high-resolution, offshore west of Hawai‘i. Additionally, we present plume-scale salinity distribution and freshwater volumetric estimation.

STUDY AREA

The Kailua-Kona region situated along the west coast of the Hawai‘i island is bounded from the north by the northwest rift zone of the Hualalai Volcano, and from the east by the south-southeast rift zone of Hualalai Volcano and by the southwest rift zone of Mauna Loa Volcano (Figure 1). Extensive aquifers on the island of Hawai‘i were formed consequently to volcanic eruptions during the initial building stage of each volcano (e.g., Gingerich and Oki, 2000). These volcanic eruptions are characterized by lava flows, faults, dikes, ash beds, lava tubes, and pyroclastic deposits, which formed the terrestrial aquifers situated on the Island of Hawai‘i (Oki, 1999; Gingerich and Oki, 2000). The permeability of these volcanic rocks depends on the mode of emplacement, rocks thickness, and the amount of weathering. The abundance of lava tubes at this region increases the permeability of the volcanic rocks thereby promoting the formation of large aquifers (e.g., Oki, 1999; Gingerich and Oki, 2000).

In the land-to-sea transition zone, groundwater in Hawai‘i is typically present as a thin freshwater basal lens overlying seawater (Stearns and Macdonald, 1942; Gingerich, 2008). The shallow offshore region surveyed in this study (parallel to the Hualalai terrestrial aquifer) is composed of subaerial alkalic lava flow drapes, intermediately covered by coral reef terraces with low sediment content (Moore and Clague, 1987; Taylor, 2019), as shown in Figure A-1. This regional volcanic formation [fractures, faults, porous basalts, and lava tubes, (Oki, 1999; Gingerich and Oki, 2000)], enables the direct flow of submarine groundwater from the subsurface to the water-column, manifested as SGD.

DATA ACQUISITION AND PROCESSING

In this marine survey, we collected CSEM data using a newly developed surface-towed CSEM system (Figure 2) to image the electrical structure of the submerged flank of the Hualalai volcano (Attias et al., 2019) and the water-column offshore west of Hawai‘i. Our survey included ten towlines parallel to the Hualalai terrestrial aquifer at incremental distances from the Kailua-Kona coastline (inline tows), and two perpendicular towlines (crossline tows), covering an offshore region of about 4 km wide and 40 km long, producing ~200 km of continuous CSEM data (Figure 1).

The surface-towed CSEM system employs a 40 m-long dipole antenna at ~0.5 m behind the survey boat, towed at an average speed of 3.5 knots while transmitting a 100 A current using a doubly symmetric square waveform at a fundamental frequency of 1 Hz, thus, generating a source dipole moment of 5.09 kAm. Higher signal-to-noise (SNR) ratios characterize this waveform at higher frequencies than the standard square wave and other typical waveforms (Myer et al., 2011). The survey boat surface-towed four broadband electromagnetic

(EM) receiver at offsets 268, 536, 804, 1072 m (Figure 2). A Dorsal unit positioned 30 m behind the EM receivers array recorded the altitude and surface water conductivity and temperature. Each EM receiver recorded the inline horizontal electric field on a 2 m dipole positioned ~0.65 m below the sea surface (Sherman et al., 2017; Gustafson et al., 2019). GPS systems and electronic compasses logged the receiver positions and orientations, respectively (Figure 2).

The recorded CSEM data were Fourier transformed into the frequency domain and stacked over 60 s intervals. This stacking corresponds to ~20 m lateral distance between transmitter stack points, producing amplitude and phase responses per receiver as a function of position and frequency harmonics. The stacked amplitude and phase responses were then merged with the transmitter and receivers navigational information. For our CSEM inversion, we used the strongest harmonics of the doubly symmetric square waveform (Myer et al., 2011), here corresponds to frequencies of 1, and 7 Hz. These two frequencies produced high-quality data, lowest SNR, and high sensitivity to the resistivity structure of the water-column and the shallow sub-seafloor (Attias et al., 2019).

123

CSEM INVERSION PARAMETERIZATION

To invert the CSEM data for electrical resistivity, we employed the open-source MARE2DEM code, a 2-D nonlinear regularized inversion method that uses a parallel goal-oriented adaptive finite-element algorithm (Key and Ovalle, 2011; Key, 2016). MARE2DEM uses Occam's inversion, which searches for the smoothest model that fits the data to a predefined root-mean-square (RMS) target misfit (Constable et al., 1987). The CSEM inversion-starting model discretization includes a $10^{13} \Omega\text{m}$ air layer as a fixed-parameter, followed by finely discretized ($20 \text{ m} \times 10 \text{ m}$) quadrilateral mesh (Key, 2016) for the water-column (free parameters with half-space starting resistivity = $0.2 \Omega\text{m}$), and fine mesh elements ($1000 \text{ m} \times 10 \text{ m}$), defined as free parameters (half-space starting resistivity = $10 \Omega\text{m}$), as shown in Figure B-1.

High-resolution ($2 \text{ m} \times 2 \text{ m}$) multi-beam system (Figure A-1) recorded the bathymetry used in the CSEM inversion modeling. The 40 m-long dipole transmitter and the 2 m-long towed CSEM receiver dipoles (Figure 2), were modeled as finite dipole lengths. Our finite dipole inversions produced models with high sensitivity of the data to model parameters (Figure 4b). The inversions' horizontal to vertical roughness vary between 2 and 10 as a function of width-to-depth ratio. All of our CSEM inversion models fit the data to an RMS misfit of 1.0 with adequate model-to-data fits, yielding minimal and randomly distributed normalized residuals (Figures C-1, and C-2).

RESULTS

The electrical structure of the sub-seafloor offshore west of Hawai'i using all the survey lines shown in Figure 1 is described in Attias et al. (2019). Here, we focus on 2-D isotropic inversion modeling of the water-column using CSEM data collected at four sections of survey line 3 (Figure 1). Our CSEM models image the electrically resistive of freshwater plumes in high resolution and detect anomalous resistive regions near the sea-surface, indicative of large freshwater bodies (Figures 3–6).

147 Electrical imaging of freshwater plumes

148 The CSEM inversion model of line 3a (located \sim 2.3 km from the shoreline) show a resistive
149 anomaly (\sim 2.5 Ω m; the background resistivity of the seawater is \sim 0.2–0.4 Ω m) that
150 extends from the seafloor to the sea-surface, which we interpret as a moderate freshwater
151 plume (Figure 3). This plume is fed by a sub-seafloor freshwater deposit situated between
152 \sim 150 m to \sim 250 m depth. The plume is \sim 1 km wide at the seafloor and \sim 20 m at the
153 surface (Figure 3).

154 Line 3b (located \sim 2 km from the shoreline) CSEM inversion model presents a fresh-
155 water plume with varying electrical resistivity, ranging from \sim 2 Ω m near the seafloor to
156 \sim 25 Ω m at the sea-surface (Figure 4a). This plume is \sim 60 m wide at the seafloor and
157 \sim 130 m near the surface. From both flanks of the model, two laterally elongated resistive
158 anomalies (\sim 30 Ω m) extends from the surface to a depth of \sim 15 m, indicating the presence
159 of surface freshwater. These two surface freshwater bodies most likely emerge from nearby
160 plumes, as they are disconnected from Line 3b plume (Figure 4a). The Jacobian sensitivity
161 matrix (e.g., Farquharson and Oldenburg, 1996; MacGregor et al., 2001) derived from line
162 3b model, demonstrate high data sensitivity to model parameters across the entire water-
163 column (Figure 4b). Such a high data sensitivity to water-column model parameters found
164 in all of our inversion models. The model-to-data fit and normalized residuals of Line 3b
165 inversion are shown in Figure C-1.

166 Similar to the inversion model of line 3b, line 3c model (located \sim 1–2 km from the
167 shoreline) also exhibits a central vertically elongated freshwater plume (resistivity ranges
168 between \sim 1–5 Ω m) and two laterally extensive surface freshwater bodies showing resistivity
169 of \sim 30 Ω m (Figure 5). This plume is \sim 1 km wide at the seafloor and \sim 60 m near the
170 surface. The surface freshwater body at the northwest flank of the model in unconnected
171 to the central plume, however, the southeast freshwater body, is moderately linked to the
172 plume. However, the resistivity of the southeast freshwater body is six times higher than
173 the surface resistivity of the plume (Figure 5). This suggests that the southeast freshwater
174 body accumulates freshwater from nearby plumes as well as a moderate influx from line 3c
175 plume. Figure C-2 shows the model-to-data fit and normalized residuals of line 3c inversion.

176 The inversion model of line 3d (located \sim 0.5–1 km from the shoreline) presents a promi-
177 nent freshwater plume that is laterally extensive (\sim 100 m wide) near at the seafloor and
178 surface but narrows at its center. The highest resistivity of this plume (\sim 30 Ω m) is between
179 the surface and \sim 25 m water depth, whereas near the seafloor, the resistivity is \sim 5 Ω m.
180 The sub-seafloor freshwater deposit and the freshwater plume in the water-column appear
181 to be intrinsically linked. However, the high resistivity detected near the sea-surface might
182 occur due to freshwater fluxes from nearby plumes (Figure 6). At the northwest flank of the
183 model, \sim 30 Ω m resistive anomaly exist between the surface and \sim 15 m depth, extending
184 horizontally about 180 m. This surface freshwater body is disconnected from the line 3d
185 plume, thus, representing freshwater that emerged from the seafloor elsewhere and drifted
186 to the vicinity of survey line 3d.

187 Plume salinity distribution and freshwater content**DISCUSSION**

188 Global utilization of sizeable submarine groundwater reserves can assist in mitigating the
189 adverse effects of onshore pumping, which are commonly manifested by seawater intrusion
190 (e.g., Galloway and Burbey, 2011; Bakken *et al.*, 2012; Ferguson and Gleeson, 2012).
191 Thus, ideally, expand the hydrological boundaries towards the offshore domain (Post *et al.*,
192 2013). Coastal aquifers are one of Hawai‘i’s most critical natural resources, providing the
193 vast majority of water for drinking, irrigation, domestic, commercial, and industrial needs
194 (Gingerich and Oki, 2000). Due to the constant decrease in rainfall, increase in population,
195 tourism, and industrial demands on the island of Hawai‘i, exploring viable alternative
196 sources of freshwater is essential.

197 Multiple point-source SGD locations offshore west of Hawai‘i are most likely linked
198 to inland lava flows formations (Peterson *et al.*, 2009; Dimova *et al.*, 2012), manifested
199 by subsurface laterally continuous freshened groundwater reservoirs (Attias *et al.*, 2019).
200 Multichannel electrical resistivity measurements (Dimova *et al.*, 2012) provide evidence for
201 substantial SGD at the Kiholo Bay (Figure 1). Calculation of SGD rates at Kiholo Bay
202 from surface thermal infrared imagery and point-source measurements suggests a total dis-
203 charge that ranges between 8,600 m³/d (Johnson *et al.*, 2008) and 9,200 m³/d (Dimova
204 *et al.*, 2012). Because rates of fresh SGD are highly heterogeneous, plume seepage loca-
205 tion and spatiotemporal estimates are essential for predicting threats to water quality at
206 coastal aquifers, land-sea boundary, and marine surface waters (Sawyer *et al.*, 2016). Our
207 regional-scale CSEM mapping offshore west of Hawai‘i shows the exact location and spatial
208 distribution of individual SGD plumes from the seafloor to the sea surface, thus enabling
209 the assessment of the effects of fresh SGD fluxes both on localized and regional scales.

CONCLUSIONS

210 Spatiotemporal variability of fresh SGD at coastal waters alters oceanographic, hydrogeo-
211 logical, and biogeochemical processes on both local and regional scales. Various geophysical,
212 geochemical, and bio-ecological studies suggest that surface SGD nearshore west of Hawai‘i
213 is distributed diffusively on a large regional-scale. This study demonstrates the capability
214 of the CSEM method to image and delineate freshwater plumes from the seafloor to surface
215 in high-resolution, offshore west of Hawai‘i. Our findings reveal multiple fresh SGD plumes,
216 most likely fed by freshwater submarine accumulations. Plume-scale salinity distribution
217 shows that a significant volume of freshwater accommodates the plumes. Utilization of deep
218 submarine freshwater deposits that are most likely intrinsically linked to freshwater plumes
219 can significantly increase water availability to the island of Hawai‘i at low energetic coast
220 (due to high hydrostatic pressure), and minimal impact on coastal ecosystems.

ACKNOWLEDGMENTS

221 This study was supported via the Hawai‘i EPSCoR Program, funded by the National Science
222 Foundation Research Infrastructure Improvement Award (RII) Track-1: ‘Ike Wai: Securing
223 Hawai‘i’s Water Future Award # OIA-1557349. The authors would like to thank G. Jacobs,
224 B. Taylor, C. Voss, D. Eason, N. Maximenko, B. Powell, F. Langenberger, K. Kelly, C.

²²⁵ Gustafson, and C. Chesley for helpful discussions. We also thank the captain, crew, and
²²⁶ scientific party of survey boat Huki Pono.

APPENDIX A

REGIONAL BATHYMETRY

227 Figure A-1 shows fluctuate bathymetry with multiple seabed features, exhibiting significant
228 seafloor heterogeneity offshore west of Hawai‘i. Sharp basaltic slopes superimposed by coral
229 terraces and low sediment content characterize this region.

APPENDIX B

CSEM INVERSION STARTING MODEL

230 Figure B-1 shows an example of the CSEM inversion starting model applied in line 3b
231 inversion. Water column quadrilateral meshing: 20 m-by-10 m, sub-seafloor quadrilateral
232 meshing: 1000 m by 10 m.

APPENDIX C

INVERSIONS MODEL-TO-DATA FITS

233 Figure C-1 shows the model-to-data fit and normalized residuals of the isotropic inversion
234 applied to survey line 3b CSEM data (corresponds to Figure 4, main article).

235 Figure C-2 shows the model-to-data fit and normalized residuals of the isotropic inversion
236 applied to survey line 3c data (corresponds to Figure 5, main article).

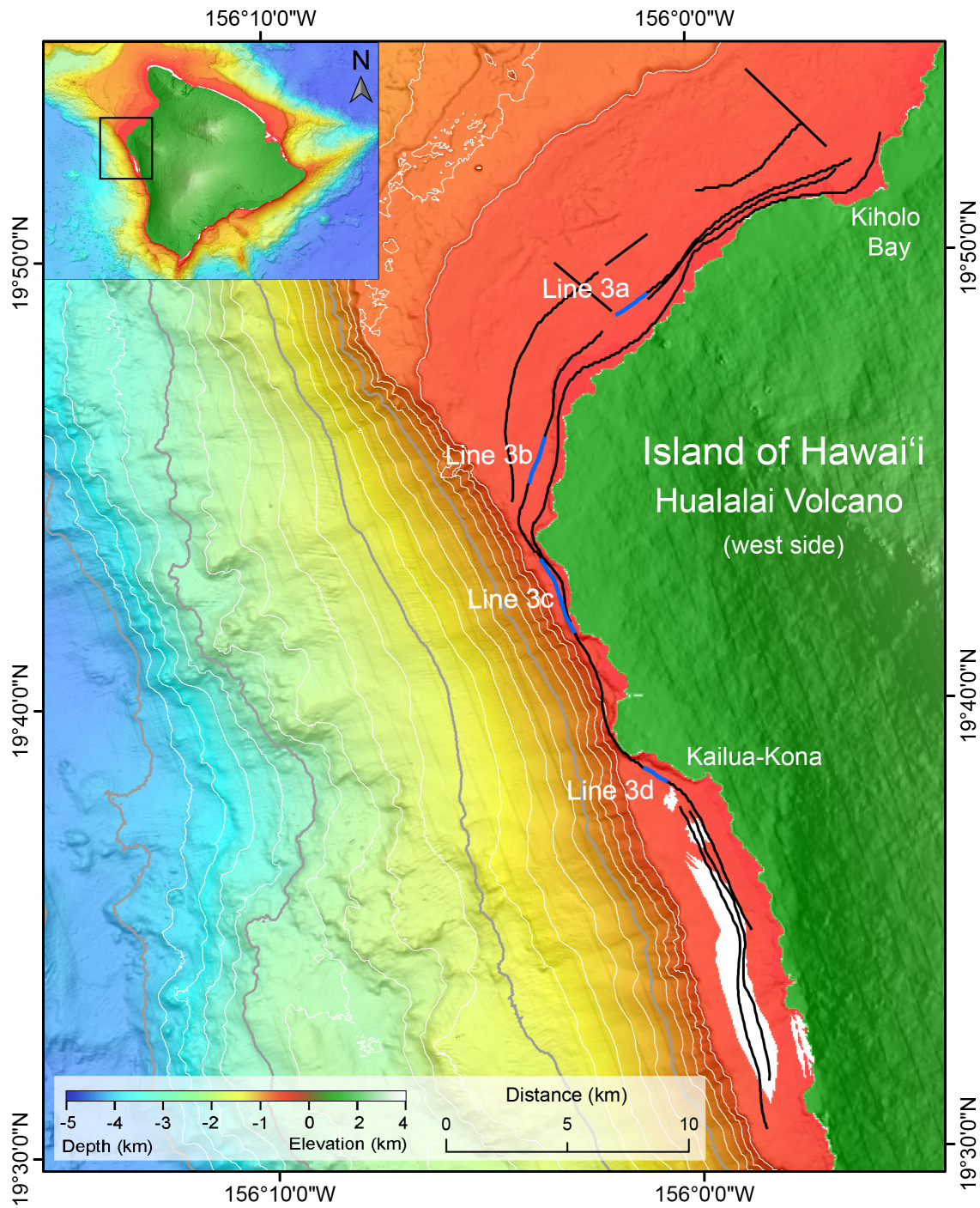


Figure 1: Map of the study area parallel to the Hualalai terrestrial aquifer at Kailua-Kona, offshore west of Hawai‘i. The black lines denote the survey towlines (10 inlines, and two crosslines). Blue lines represent regions where freshwater plumes were detected (Figures 3–6). White lines denote depth contours of 200 m, and grey lines the depth contours of 1000 m. Inset map: The Island of Hawai‘i, with a black rectangle indicating the main map area. Areas with no bathymetry data are shown in white. Bathymetry data: Courtesy of Hawai‘i Mapping Research Group.

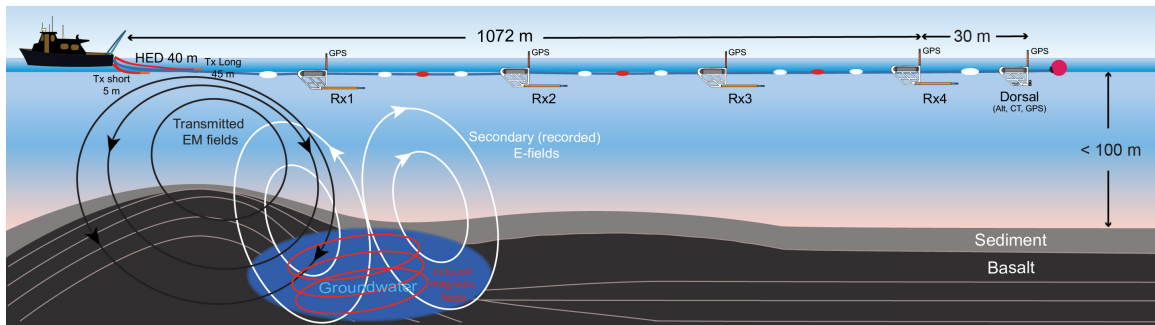


Figure 2: A schematic illustration of the surface-towed CSEM system. This system includes a 40 m horizontal electric dipole (HED) source (Tx), which emits a current of 100 A and four receivers (Rx) positioned at increment distance of ~ 250 m to form a ~ 1 km array. Each receiver includes a 2 m inline electric dipole, a data logger, and a GPS unit. At the end of the array, a Dorsal unit is located, equipped with an altimeter (Alt), conductivity/temperature (CT) measuring device, and a GPS unit. The EM laboratory at Scripps Institution of Oceanography designed and built this surface-towed CSEM system.

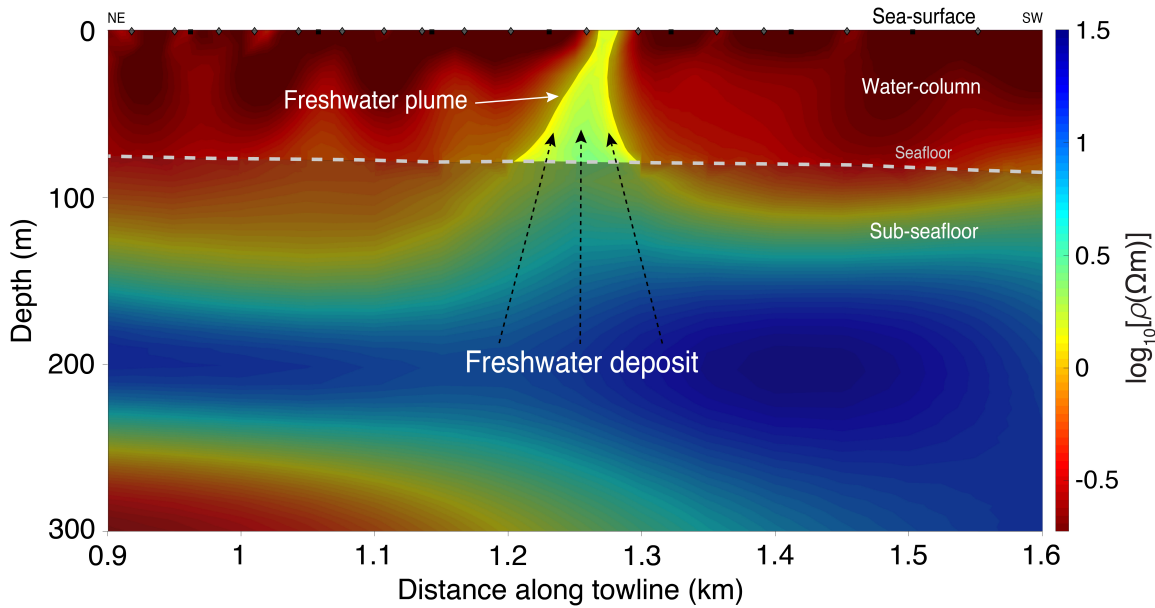


Figure 3: Two-dimensional inversion model derived from the CSEM data acquired in survey line 3a. The colour scale present the electrical resistivity in $\log_{10}[\rho(\Omega\text{m})]$. Moderate freshwater plume observed at ~ 1.25 km distance along the towline, extending from the seafloor to the sea-surface, showing an average resistivity of $\sim 2.5 \Omega\text{m}$. The model derived from the data acquired by three surface-towed CSEM receivers at 3 Hz and 7 Hz. The error floors of the amplitude and phase are 10%. This inversion converged to a root-mean-square (RMS) misfit of 1.0 after 19 iterations. The grey dashed line represents the seafloor, positioned at a water depth of ~ 85 m. Black squares and grey diamonds denote transmitter and receiver positions, respectively.

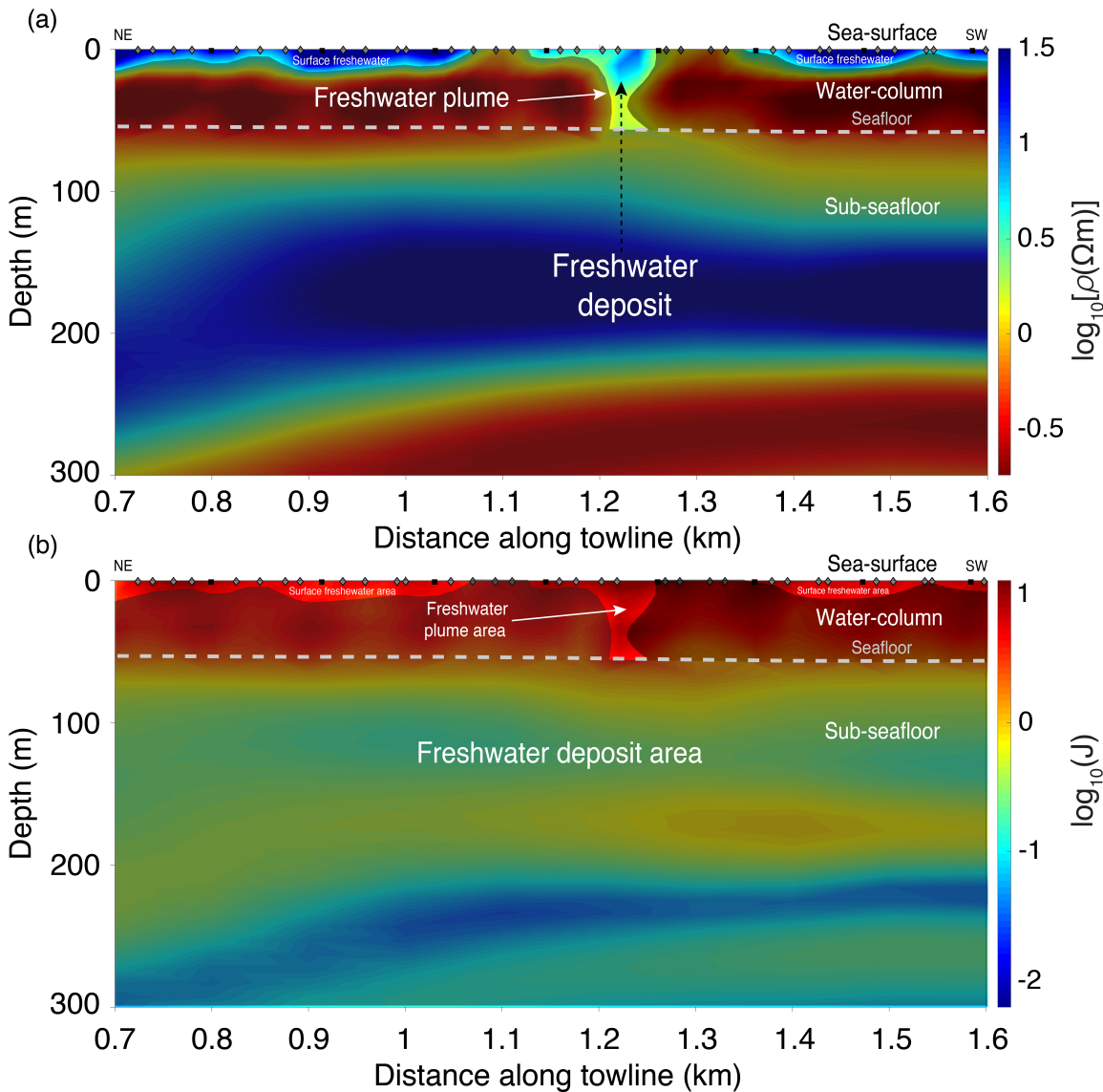


Figure 4: Two-dimensional inversion model derived from the CSEM data acquired in survey line 3b. The colour scale present the electrical resistivity in $\log_{10}[\rho(\Omega\text{m})]$. Distinctive freshwater plume observed at a distance of ~ 1.23 km along the towline, extending from the seafloor to the sea-surface, showing a resistivity range of ~ 2 – $25 \Omega\text{m}$. Two shallow lateral resistive anomalies ($\sim 30 \Omega\text{m}$) from both flanks of the model represent surface freshwater bodies. The model derived from the data acquired by four surface-towed CSEM receivers at 3 Hz and 7 Hz, and fit to RMS of 1.0 after 12 iterations, with error floors of 8% for the amplitude and phase data. The grey dashed line represents the seafloor, positioned at a water depth of ~ 50 m. Black squares and grey diamonds denote transmitter and receiver positions, respectively. (b) Model showing the data sensitivities derived from the inversion model of line 3b. The sensitivity matrix evaluates the data sensitivity to model parameters. The total sensitivities were computed as sums over all data points and normalized by data deviation and cell area. Black squares and grey diamonds denote transmitter and receiver positions, respectively.

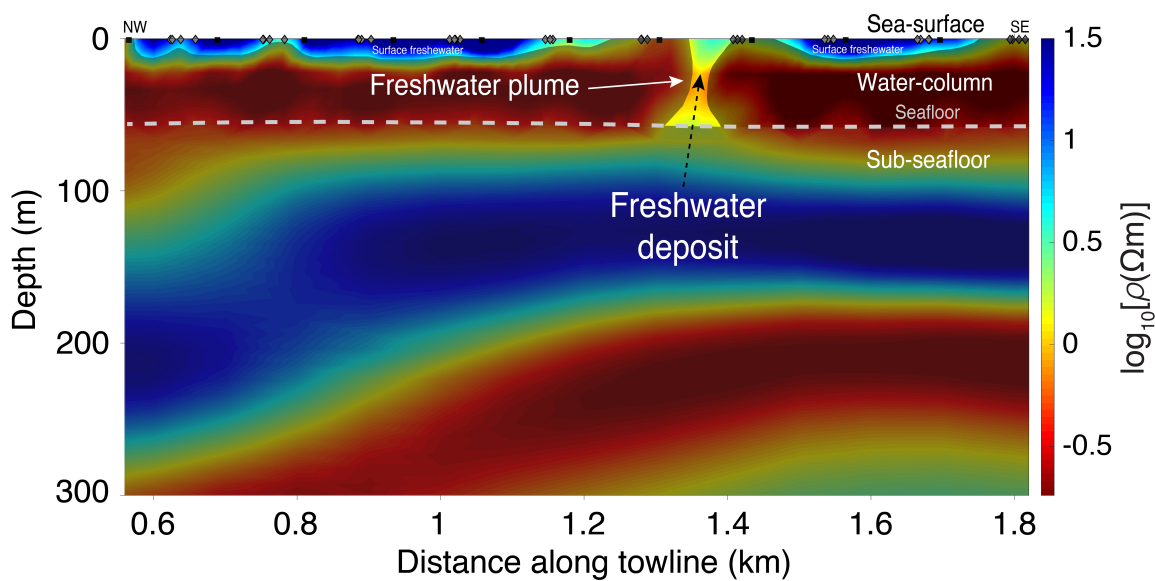


Figure 5: Two-dimensional inversion model derived from the CSEM data acquired in survey line 3c. The colour scale present the electrical resistivity in $\log_{10}[\rho(\Omega\text{m})]$. Moderate freshwater plume observed at a distance of ~ 1.35 km along the towline, extending from the seafloor to the sea-surface, showing a resistivity range of $\sim 1\text{--}5 \Omega\text{m}$. Two shallow lateral resistive anomalies ($\sim 30 \Omega\text{m}$) from both flanks of the model represent surface freshwater bodies. The model derived from the data acquired by three surface-towed CSEM receivers at 3 Hz and 7 Hz, and fit to RMS of 1.0 after 14 iterations, with error floors of 8% and 6% for the amplitude and phase data, respectively. The grey dashed line represents the seafloor, positioned at a water depth of ~ 60 m. Black squares and grey diamonds denote transmitter and receiver positions, respectively.

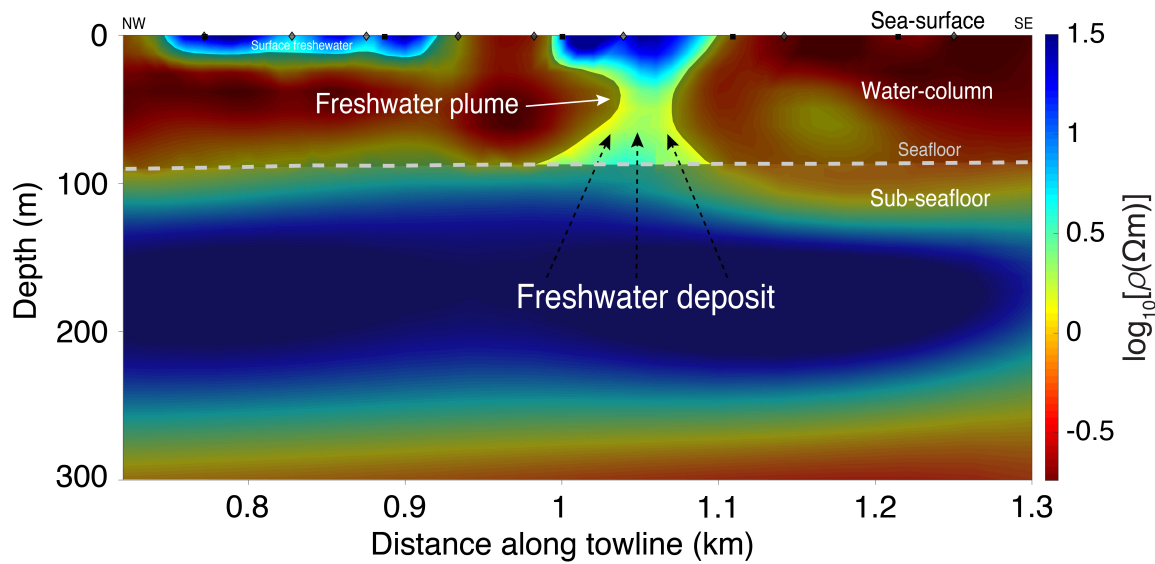


Figure 6: Two-dimensional inversion model derived from the CSEM data acquired in survey line 3d. The colour scale present the electrical resistivity in $\log_{10}[\rho(\Omega\text{m})]$. Distinctive freshwater plume observed between ~ 1 – 1.1 km distance along the towline, extending from the seafloor to the sea-surface, showing a resistivity range of ~ 2.5 – $30 \Omega\text{m}$. A shallow lateral resistor ($\sim 30 \Omega\text{m}$) at the left flank of the model represents a surface freshwater body. The model derived from the data acquired by three surface-towed CSEM receivers at 3 Hz and 7 Hz, and fit to RMS of 1.0 after 15 iterations, with error floors of 9% and 7% for the amplitude and phase data, respectively. The grey dashed line represents the seafloor, positioned at a water depth of ~ 95 m. Black squares and grey diamonds denote transmitter and receiver positions, respectively.

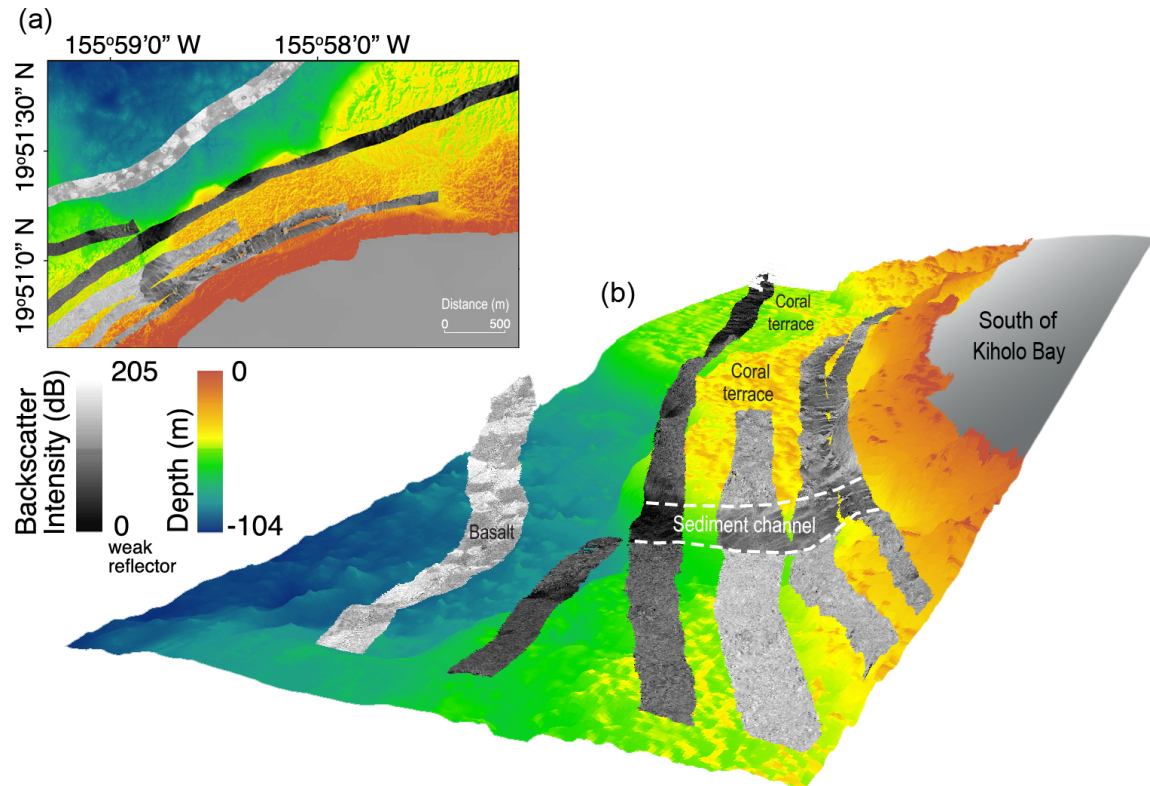


Figure A-1: An example of the high-resolution ($\sim 2 \times 2$ m) multi-beam and backscatter data collected using the R2Sonic2024 system. (a) Multi-beam and backscatter data in a 2-D view, (b) Multi-beam and backscatter data in a 3-D view.

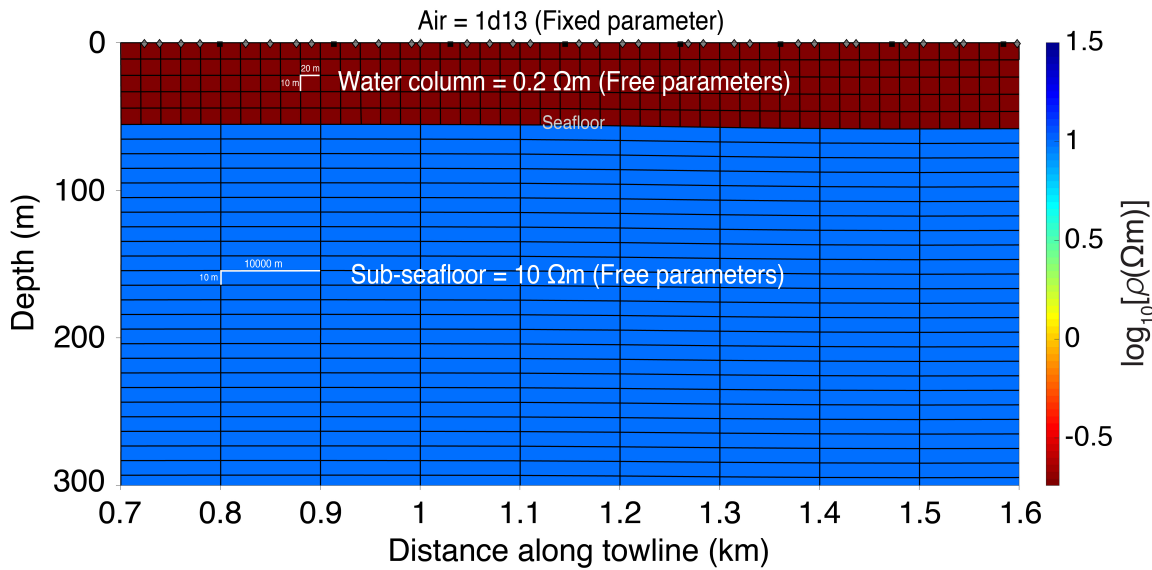


Figure B-1: The CSEM inversion-starting model discretization. The colour scale present the half-space starting electrical resistivity in $\log_{10}[\rho(\Omega\text{m})]$. Black lines represent the quadrilateral mesh discretization applied to the seawater column and the sub-seafloor region of interest. Black squares and grey diamonds denote transmitter and receiver positions, respectively.

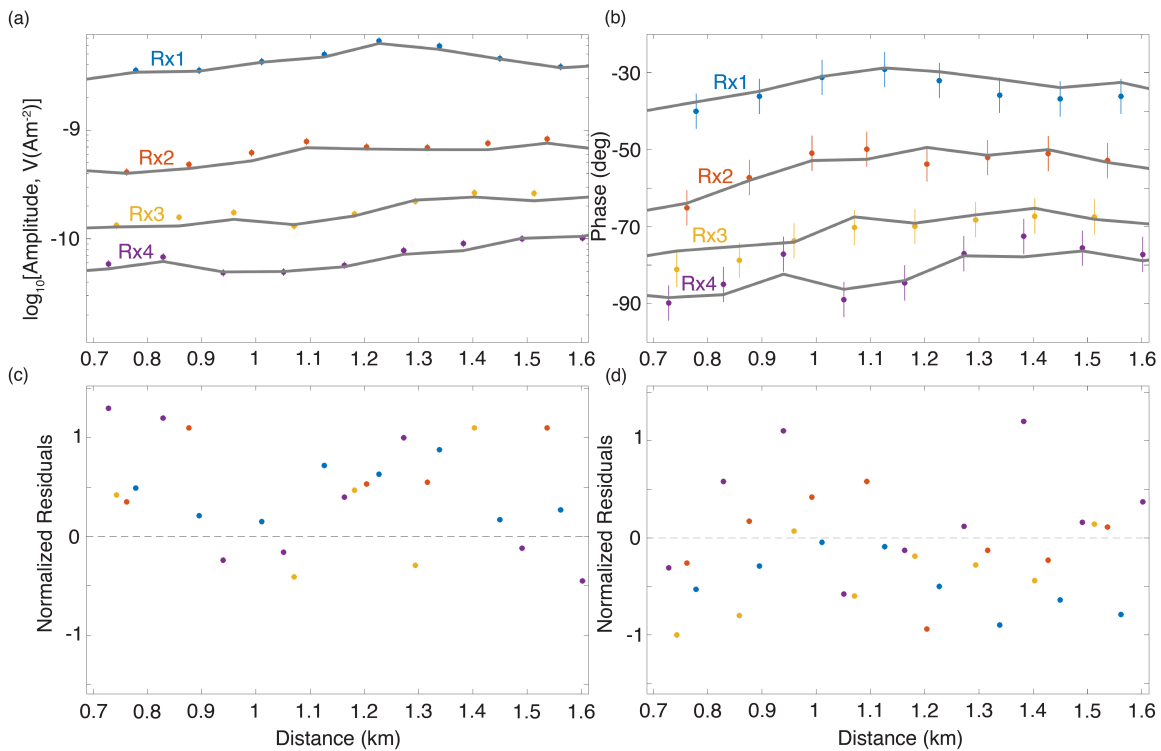


Figure C-1: The model-to-data fit and normalized residuals derived from line 3b CSEM inversion using four surface-towed receivers (Rx1, Rx2, Rx3, Rx4 [Tx-Rx offsets shown in Figure 2]). (a) Amplitude model-to-data fit at 7 Hz, (b) Phase model-to-data fit at 7 Hz. The grey lines represent the model responses, dots the data, and vertical lines the associated uncertainty bars. Panels (c) and (d) denote the amplitude and phase normalized residuals, respectively. Note the minimal and randomly distributed normalized residuals.

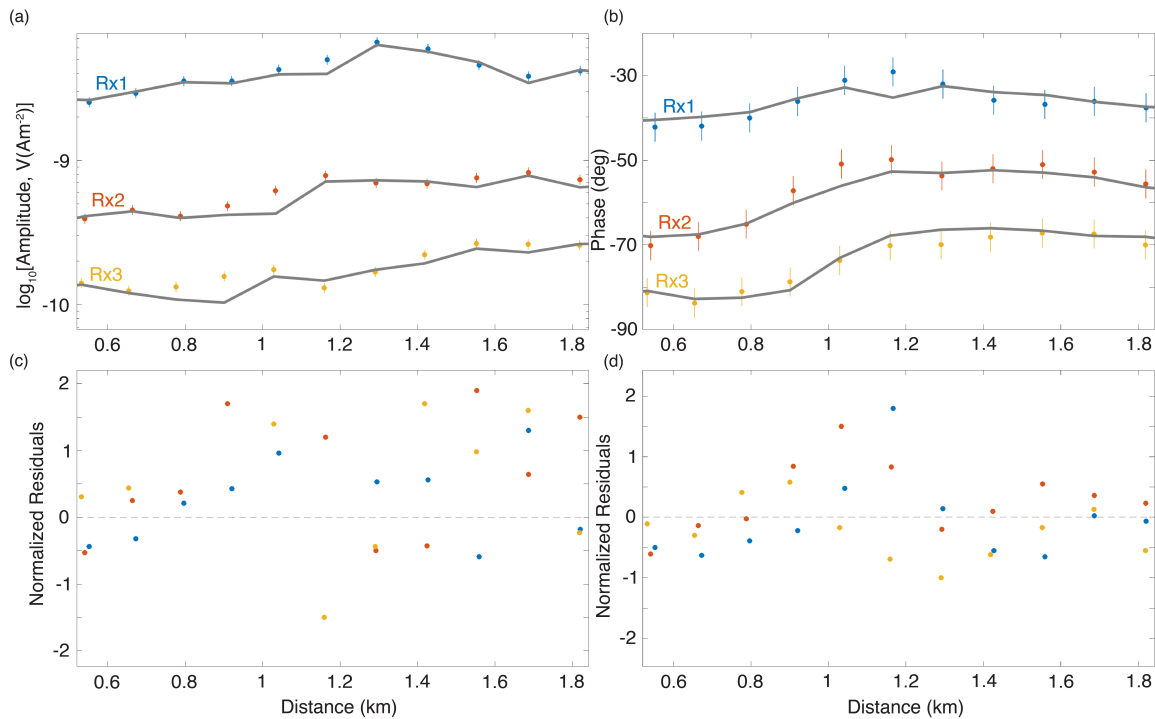


Figure C-2: The model-to-data fit and normalized residuals derived from line 3c CSEM inversion using three surface-towed receivers (Rx1, Rx2, Rx3 [Tx-Rx offsets shown in Figure 2]). (a) Amplitude model-to-data fit at 7 Hz, (b) Phase model-to-data fit at 7 Hz. The grey lines represent the model responses, dots the data, and vertical lines the associated uncertainty bars. Panels (c) and (d) denote the amplitude and phase normalized residuals, respectively. Note the minimal and randomly distributed normalized residuals.

REFERENCES

- 237 Attias, E., D. Sherman, K. Ismail, and S. Constable, 2019, Controlled-source Electromagnetic Imaging of Submarine Groundwater Reservoirs Offshore the Island of Hawai'i: Presented at the AGU Fall Meeting 2019, AGU.
- 238
- 239
- 240 Bakken, T. H., F. Ruden, and L. E. Mangset, 2012, Submarine groundwater: a new concept for the supply of drinking water: *Water Resour. Manage.*, **26**, 1015–1026.
- 241
- 242 Burnett, W., P. Aggarwal, A. Aureli, H. Bokuniewicz, J. Cable, M. Charette, E. Kontar, S. Krupa, K. Kulkarni, A. Loveless, et al., 2006, Quantifying submarine groundwater discharge in the coastal zone via multiple methods: *Sci. Total Environ.*, **367**, 498–543.
- 243
- 244 Church, T. M., 1996, An underground route for the water cycle: *Nature*, **380**, 579–580.
- 245
- 246 Cohen, D., M. Person, P. Wang, C. W. Gable, D. Hutchinson, A. Marksamer, B. Dugan, H. Kooi, K. Groen, D. Lizarralde, et al., 2010, Origin and extent of fresh paleowaters on the Atlantic continental shelf, USA: *Groundwater*, **48**, 143–158.
- 247
- 248
- 249 Constable, S., 2010, Ten years of marine CSEM for hydrocarbon exploration: *Geophysics*, **75**, 67–81.
- 250
- 251 Constable, S. C., R. L. Parker, and C. G. Constable, 1987, Occam's inversion: A practical algorithm for generating smooth models from electromagnetic sounding data: *Geophysics*, **52**, 289–300.
- 252
- 253 Cyronak, T., I. R. Santos, D. V. Erler, and B. D. Eyre, 2013, Groundwater and porewater as major sources of alkalinity to a fringing coral reef lagoon (Muri Lagoon, Cook Islands): *Biogeosciences*, **10**, 2467.
- 254
- 255 De Carlo, E., 1992, Geochemistry of pore water and sediments recovered from the Exmouth Plateau: *Proc. Ocean Drill. Program*, 295–308.
- 256
- 257 Dimova, N. T., P. W. Swarzenski, H. Dulaiova, and C. R. Glenn, 2012, Utilizing multichannel electrical resistivity methods to examine the dynamics of the fresh water–seawater interface in two Hawaiian groundwater systems: *J. Geophys. Res.*, **117**, 10.1029/2011JC007509.
- 258
- 259 Duarte, T. K., H. F. Hemond, D. Frankel, and S. Frankel, 2006, Assessment of submarine groundwater discharge by handheld aerial infrared imagery: Case study of Kaloko fishpond and bay, Hawai'i: *Limnol. Oceanogr.*, **4**, 227–236.
- 260
- 261 Dulai, H., J. Kamenik, C. A. Waters, J. Kennedy, J. Babinec, J. Jolly, and M. Williamson, 2016, Autonomous long-term gamma-spectrometric monitoring of submarine groundwater discharge trends in Hawaii: *J. Radioanal. Nucl. Chem.*, **307**, 1865–1870.
- 262
- 263 Edwards, N., 2005, Marine controlled source electromagnetics: principles, methodologies, future commercial applications: *Surv. Geophys.*, **26**, 675–700.
- 264
- 265 Evans, R., and K. Key, 2016, Mapping Offshore Freshwater Deposits Using Electromagnetic Methods: Near Surface Geoscience 2016 - Second Applied Shallow Marine Geophysics Conference, 10.3997/2214-4609.201602169.
- 266
- 267 Farquharson, C., and D. Oldenburg, 1996, Approximate sensitivities for the electromagnetic inverse problem: *Geophys. J. Int.*, **126**, 235–252.
- 268
- 269 Ferguson, G., and T. Gleeson, 2012, Vulnerability of coastal aquifers to groundwater use and climate change: *Nature Clim. Change*, **2**, 342.
- 270
- 271 Galloway, D. L., and T. J. Burbey, 2011, Regional land subsidence accompanying groundwater extraction: *Hydrogeol. J.*, **19**, 1459–1486.
- 272
- 273 Gingerich, S. B., 2008, Ground-water availability in the Wailuku Area, Maui, Hawai'i: Technical report, US Geological Survey.
- 274
- 275 Gingerich, S. B., and D. S. Oki, 2000, Ground water in hawaii: Technical report, US

- 283 Geological Survey.
- 284 Gleick, P. H., and M. Palaniappan, 2010, Peak water limits to freshwater withdrawal and
285 use: *Proceedings of the National Academy of Sciences*, **107**, 11155–11162.
- 286 Grasby, S. E., Z. Chen, D. Issler, and L. Stasiuk, 2009, Evidence for deep anaerobic biodegra-
287 dation associated with rapid sedimentation and burial in the Beaufort–Mackenzie basin,
288 Canada: *Appl. Geochem.*, **24**, 536–542.
- 289 Gustafson, C., K. Key, and R. L. Evans, 2019, Aquifer systems extending far offshore on
290 the US Atlantic margin: *Sci. Rep.*, **9**, 1–10.
- 291 Haroon, A., K. Lippert, V. Mogilatov, and B. Tezkan, 2018, First application of the marine
292 differential electric dipole for groundwater investigations: A case study from Bat Yam,
293 Israel: *Geophysics*, **83**, B59–B76.
- 294 Hathaway, J. C., C. W. Poag, P. C. Valentine, F. T. Manheim, F. A. Kohout, M. H. Bothner,
295 R. E. Miller, D. M. Schultz, and D. A. Sangrey, 1979, US Geological Survey core drilling
296 on the Atlantic shelf: *Science*, **206**, 515–527.
- 297 Jiao, J. J., L. Shi, X. Kuang, C. M. Lee, W. W.-S. Yim, and S. Yang, 2015, Reconstructed
298 chloride concentration profiles below the seabed in Hong Kong (China) and their impli-
299 cations for offshore groundwater resources: *Hydrogeol. J.*, **23**, 277–286.
- 300 Johannes, R., 1980, The ecological significance of the submarine discharge of groundwater:
301 *Mar. Ecol. Prog. Ser.*, 365–373.
- 302 Johnson, A. G., C. R. Glenn, W. C. Burnett, R. N. Peterson, and P. G. Lucey, 2008, Aerial
303 infrared imaging reveals large nutrient-rich groundwater inputs to the ocean: *Geophys.
304 Res. Lett.*, **35**.
- 305 Johnston, R. H., 1983, The saltwater-freshwater interface in the Tertiary limestone aquifer,
306 southeast Atlantic outer-continental shelf of the USA: *J. Hydrol.*, **61**, 239–249.
- 307 Key, K., 2016, MARE2DEM: a 2-D inversion code for controlled-source electromagnetic
308 and magnetotelluric data: *Geophys. J. Int.*, **207**, 571–588.
- 309 Key, K., and J. Oval, 2011, A parallel goal-oriented adaptive finite element method for
310 2.5-D electromagnetic modelling: *Geophys. J. Int.*, **186**, 137–154.
- 311 Kim, I., and G. Kim, 2011, Large fluxes of rare earth elements through submarine ground-
312 water discharge (SGD) from a volcanic island, Jeju, Korea: *Mar. Chem.*, **127**, 12–19.
- 313 Knee, K. L., E. D. Crook, J. L. Hench, J. J. Leichter, and A. Paytan, 2016, Assessment of
314 submarine groundwater discharge (SGD) as a source of dissolved radium and nutrients
315 to Moorea (French Polynesia) coastal waters: *Estuar. Coast.*, **39**, 1651–1668.
- 316 Knight, A. C., A. D. Werner, and L. K. Morgan, 2018, The onshore influence of offshore
317 fresh groundwater: *J. Hydrol.*, **561**, 724–736.
- 318 Lippert, K., and B. Tezkan, 2020, On the exploration of a marine aquifer offshore Israel by
319 long-offset transient electromagnetics: *Geophys. Prospect.*, **68**, 999–1015.
- 320 Luijendijk, E., T. Gleeson, and N. Moosdorf, 2020, Fresh groundwater discharge insignificant
321 for the worlds oceans but important for coastal ecosystems: *Nat. Commun.*, **11**, 1–12.
- 322 MacGregor, L., M. Sinha, and S. Constable, 2001, Electrical resistivity structure of the Valu
323 Fa Ridge, Lau Basin, from marine controlled-source electromagnetic sounding: *Geophys.
324 J. Int.*, **146**, 217–236.
- 325 Micallef, A., M. Person, A. Haroon, B. A. Weymer, M. Jegen, K. Schwalenberg, Z. Faghih,
326 S. Duan, D. Cohen, J. J. Mountjoy, et al., 2020, 3D characterisation and quantification
327 of an offshore freshened groundwater system in the Canterbury Bight: *Nat. Commun.*,
328 **11**, 1–15.
- 329 Moore, J. G., and D. Clague, 1987, Coastal lava flows from Mauna Loa and Hualalai
330 volcanoes, Kona, Hawaii: *Bull. Volcanol.*, **49**, 752–764.

- 331 Moore, W. S., 2010, The effect of submarine groundwater discharge on the ocean: Annu.
332 Rev. Mar. Sci., **2**, 345–347.
- 333 Moosdorf, N., and T. Oehler, 2017, Societal use of fresh submarine groundwater discharge:
334 An overlooked water resource: Earth-Sci. Rev., **171**, 338–348.
- 335 Mora, G., 2005, Isotope-tracking of pore water freshening in the fore-arc basin of the Japan
336 Trench: Mar. geol., **219**, 71–79.
- 337 Müller, H., T. von Dobeneck, W. Nehmiz, and K. Hamer, 2011, Near-surface electromagnetic,
338 rock magnetic, and geochemical fingerprinting of submarine freshwater seepage at
339 Eckernförde Bay (SW Baltic Sea): Geo-Mar. Lett., **31**, 123–140.
- 340 Myer, D., S. Constable, and K. Key, 2011, Broad-band waveforms and robust processing
341 for marine CSEM surveys: Geophys. J. Int., **184**, 689–698.
- 342 Oki, D. S., 1999, Geohydrology and numerical simulation of the ground-water flow system
343 of Kona, island of Hawaii: Technical report, Geological Survey (US).
- 344 Paldor, A., O. Katz, E. Aharonov, Y. Weinstein, M. Roditi-Elasar, A. Lazar, and B. Lazar,
345 2019, Deep submarine groundwater discharge—Evidence from Achziv Submarine Canyon
346 at the exposure of the Judea Group confined aquifer, eastern Mediterranean: J. Geophys.
347 Res.
- 348 Person, M., B. Dugan, J. B. Swenson, L. Urbano, C. Stott, J. Taylor, and M. Willett,
349 2003, Pleistocene hydrogeology of the Atlantic continental shelf, New England: Geological
350 Society of America Bulletin, **115**, 1324–1343.
- 351 Peterson, R. N., W. C. Burnett, C. R. Glenn, and A. G. Johnson, 2009, Quantification of
352 point-source groundwater discharges to the ocean from the shoreline of the Big Island,
353 Hawaii: Limnology and Oceanography, **54**, 890–904.
- 354 Post, V. E., J. Groen, H. Kooi, M. Person, S. Ge, and W. M. Edmunds, 2013, Offshore
355 fresh groundwater reserves as a global phenomenon: Nature, **504**, 71.
- 356 Prakash, R., K. Srinivasamoorthy, S. Gopinath, and K. Saravanan, 2018, Measurement
357 of submarine groundwater discharge using diverse methods in Coleroon Estuary, Tamil
358 Nadu, India: Appl. Water Sci., **8**, 13.
- 359 Rosenberry, D. O., C. Duque, and D. R. Lee, 2020, History and evolution of seepage meters
360 for quantifying flow between groundwater and surface water: Part 1—Freshwater settings:
361 Earth-Sci Rev., 103167.
- 362 Sawyer, A. H., C. H. David, and J. S. Famiglietti, 2016, Continental patterns of submarine
363 groundwater discharge reveal coastal vulnerabilities: Science, **353**, 705–707.
- 364 Sherman, D., P. Kannberg, and S. Constable, 2017, Surface towed electromagnetic system
365 for mapping of subsea Arctic permafrost: Earth Planet. Sci. Lett., **460**, 97–104.
- 366 Slomp, C. P., and P. Van Cappellen, 2004, Nutrient inputs to the coastal ocean through
367 submarine groundwater discharge: controls and potential impact: J. Hydrol., **295**, 64–86.
- 368 Stearns, H. T., and G. A. Macdonald, 1942, Geology and ground-water resources of the
369 island of Maui, Hawaii: Hawaii Div. Hydrogr., 344.
- 370 Stieglitz, T., 2005, Submarine groundwater discharge into the near-shore zone of the Great
371 Barrier Reef, Australia: Mar. Pollut. Bull., **51**, 51–59.
- 372 Taniguchi, M., H. Dulai, K. M. Burnett, I. R. Santos, R. Sugimoto, T. Stieglitz, G. Kim,
373 N. Moosdorf, and W. Burnett, 2019, Submarine Groundwater Discharge: Updates on its
374 Measurement Techniques, Geophysical Drivers, Magnitudes and Effects: Front. Environ.
375 Sci., **7**, 141.
- 376 Taylor, B., 2019, Shoreline slope breaks revise understanding of Hawaiian shield volcanoes
377 evolution: Geochem. Geophys. Geosyst., **20**, 4025–4045.
- 378 van Geldern, R., T. Hayashi, M. E. Böttcher, M. J. Mottl, J. A. Barth, and S. Stadler,

- 379 2013, Stable isotope geochemistry of pore waters and marine sediments from the New
380 Jersey shelf: Methane formation and fluid origin: Geosphere, **9**, 96–112.
381 Varma, S., and K. Michael, 2012, Impact of multi-purpose aquifer utilisation on a variable-
382 density groundwater flow system in the Gippsland Basin, Australia: Hydrogeol. J., **20**,
383 119–134.